



Tracking traveling ionospheric disturbances through Doppler-shifted AM radio transmissions

Claire C. Trop^{1,2}, James LaBelle², Philip J. Erickson³, Shun-Rong Zhang³, David McGaw², and Terrence Kovacs²

¹Applied Physics Laboratory, Johns Hopkins University, Laurel, MD, USA

²Department of Physics and Astronomy, Dartmouth College, Hanover, NH, USA

³Haystack Observatory, Massachusetts Institute of Technology, Westford, MA, USA

Correspondence: Claire C. Trop (claire.trop@jhuapl.edu) and James LaBelle (james.w.labelle@dartmouth.edu)

Received: 26 July 2024 – Discussion started: 26 August 2024

Revised: 11 December 2024 – Accepted: 17 January 2025 – Published: 28 April 2025

Abstract. Six specialized radio receivers were developed to measure the Doppler shift of amplitude modulation (AM) broadcast radio carrier signals due to ionospheric effects. Five were deployed approximately in a circle at a one-hop distance from an 810 kHz clear-channel AM transmitter in Schenectady, New York, and the sixth was located close to the transmitter, providing a reference recording. Clear-channel AM signals from New York City and Connecticut were also received. The experiment confirmed detection of traveling ionospheric disturbances (TIDs) and measurement of their horizontal phase velocities through monitoring variations in the Doppler shift of reflected AM signals imparted by vertical motions of the ionosphere. Comparison of 12 events with simultaneous global navigation satellite system (GNSS)-based TID measurements showed generally good agreement between the two techniques slightly more than half the time and substantial differences slightly less than half the time, with differences attributable to differing sensitivities of the techniques to wave altitude and characteristics within a complex wave environment. Detected TIDs had mostly southward phase velocities, and in four cases they were associated with auroral disturbances that could plausibly be their sources. A purely automated software technique for event detection and phase velocity measurement was developed and applied to 1 year of data, revealing that AM Doppler sounding is much more effective when using transmitter signals in the upper part of the AM band (above 1 MHz) and demonstrating that the AM Doppler technique has promise to scale to large numbers of receivers covering continent-wide spatial scales.

1 Introduction

Traveling ionospheric disturbances (TIDs) are a category of ionospheric variations characterized by propagating wave-like undulations in the ionospheric layer height and/or variations in ionospheric electron density. TIDs have been studied since the earliest days of ionospheric radio research (reviews by Hunsucker, 1982; Hocke and Schlegel, 1996). They are typically classified as medium-scale (MSTIDs), having horizontal wavelengths of hundreds of kilometers, periods of 15–60 min, and horizontal phase speeds of 250–1000 m s⁻¹, and large-scale (LSTIDs), having horizontal wavelengths exceeding 1000 km, periods of 30–180 min, and horizontal phase speeds of 400–1000 m s⁻¹ (Hernández-Pajares et al., 2012; Otsuka et al., 2013; Tsugawa et al., 2004; Ding et al., 2014). TIDs can be the ionospheric signature of atmospheric processes, such as gravity waves (review by Yeh and Liu, 1974; Francis, 1975; Fritts, 1995), or can result from electrodynamically driven ionospheric processes, such as the Perkins instability (Perkins, 1973; Cosgrove and Tsunoda, 2002, 2004; Cosgrove, 2007; Kelley, 2011; Makela and Otsuka, 2011). Atmospheric gravity waves associated with TIDs are an important mechanism of energy and momentum transport between atmospheric regions. For example, storm-time LSTIDs involve significant energy transport from high to low latitudes (Richmond, 1978; Yeh and Liu, 1974). Gravity wave energy altitudinal transport, typically from lower to higher altitudes, has significant effects on atmospheric temperature dynamics, such as determining the seasonal variation in the mesopause temperature minimum (e.g., She et al., 2022). In addition to these important effects on atmo-

spheric structure and energy/momentum flow, TIDs can significantly affect both transionospheric and subionospheric radio wave propagation, including impacting radio communications systems as discussed by authors such as Frissell et al. (2022).

TIDs have been detected by many remote-sensing methods, including ionosondes, optical cameras, global navigation satellite system (GNSS) total electron content (TEC), coherent and incoherent scatter radars, and Doppler sounding using dedicated transmitters. From the earliest investigations, radio methods using transmitters of opportunity have played a significant role. Even before TIDs were first identified, variations in radio reflection height were detected by Essen (1935), using an early installation of US national time station WWV at 5 MHz frequency, and probably represent a TID detection. A host of early studies measured and statistically characterized TIDs with the Doppler sounding method using the regular and highly stable US national timing standard signal WWV broadcast at HF frequencies from Fort Collins, Colorado, and received in Palo Alto, California (Chan and Villard, 1962; Davies, 1962; Fenwick and Villard, 1960; Sears, 1972). Similar studies at HF frequencies exploited the Canadian timing signal CHU (Toman, 1975), an Australian telecommunications timing signal (Joyner and Butcher, 1980), and the Russian timing signal RWM (Reznychenko et al., 2020). Tedd et al. (1984) observed $\sim 5^\circ$ variations on a 1 h timescale in bearing deflections on 600–1000 km paths from transmitters of opportunity in central Europe, which matched TID-based modeling. In the 1980s, several groups collaborated to measure the Japanese standard timing signal JYY on 8 MHz at multiple receivers, determining the horizontal wavelength for different frequencies in the TIDs and combining these to determine a dispersion relation which matches the theoretical prediction for waves just below the Brunt–Väisälä frequency (Shibata and Okuzawa, 1983; Tsutsui et al., 1984). Tanaka et al. (1984) used Doppler sounding of the JYY timing signal at multiple sites to investigate a mechanism of TID generation by a 1982 earthquake.

Probably the most sophisticated application of transmitters of opportunity to measure TIDs is frequency angular sounding (FAS), whereby time series variations in Doppler shift, elevation of arrival, and azimuth of arrival can be inverted with certain assumptions to reconstruct the shape of the causative corrugations on the underside of the ionosphere and their time variations. Applying this technique to a transmitter of opportunity on a 700 km path using the large antenna array at the Kharkiv radio telescope facility in Ukraine, Beley et al. (1995) obtained a remarkably detailed reconstruction of the underside of the ionosphere (their Fig. 7). Subsequent work showed that this method could work successfully with much smaller receiving systems observing a transmitter of opportunity such as CHU, suggesting that worldwide digisonde networks could be employed

to conduct FAS on a regular basis (Galushko et al., 2003; Paznukhov et al., 2012).

Two recent papers illustrate TID detection using HF and MF transmitters of opportunity not related to national timing signals. Chilcote et al. (2015) showed that observations of ~ 0.1 Hz Doppler shifts of carrier frequencies of two clear-channel AM radio stations over several 100 km paths at three receiver locations allow the detection of TIDs. The study included one event with ~ 1 h period simultaneously measured with GNSS TEC, coherent backscatter radar, and a nearby digital ionosonde (digisonde); during the event, a nearly 180° discrepancy was observed between the TID horizontal velocity inferred from spaced measurements of AM signals versus that inferred from the time history of GNSS TEC maps. Recently, Frissell et al. (2022) showed TID detection and characterization through statistics of large numbers of detected serendipitous links between amateur radio operators.

The work of Chilcote et al. (2015), and, in particular, the discrepant horizontal phase velocity measurement reported therein, inspires the study presented below. Compared to Chilcote's work, our study employs a larger number of receiver locations distributed more widely around the signal source and further develops methods of detecting and characterizing TIDs through Doppler sounding of AM radio stations using multiple receiver locations and advanced signal processing techniques. Section 2 describes the instrumentation used in this study and the places where it was deployed. Section 3 describes the methodology of TID detection and horizontal phase velocity determination. Section 4 discusses the validation of these measurements using GNSS TEC data, and Sect. 5 shows evidence for auroral sources of some of the events. Section 6 applies automated data analysis to a large amount of data, suggesting how the method can scale up to much larger numbers of receiver locations. Finally, Sect. 7 summarizes the results and suggests future directions of study.

2 Instrumentation

The TID measurement system in this study consists of several elements: antenna/preamp, GPS antenna/receiver, up-converter, software-defined radio (SDR), Raspberry Pi microcomputer, and solid-state disk drives. The antenna is a vertically oriented square magnetic double loop 45 cm on a side, mounted on an ~ 1.2 m mast. The resulting antenna pattern is a dipole with a null at zero elevation in one direction, with the capability of receiving AM signals down to relatively low elevations in almost all directions. An active preamplifier mounted on the antenna mast amplifies, band-limits, and buffers the induced signal to transmit it down ~ 30 –150 m of coaxial cable (depending on site). Figure 1a shows the antenna/preamplifier in a typical setting on the roof of an academic building. At the receiver end is a bias tee allowing preamplifier power and RF signal to be sent

on the same cable. In the receiver, the signal is upshifted by 129.6 MHz by mixing with a GPS-disciplined local oscillator signal generated in custom electronics, putting the AM broadcast band in the sampling range of the software-defined radio (SDR). The RTL-SDR (using the Realtek chipset) uses a GPS-disciplined local oscillator synthesized in custom electronics, together with associated processing software running on a Raspberry Pi microcomputer, to record in-phase and quadrature waveforms corresponding to a 1 MHz bandwidth centered on 1100 kHz, covering most of the AM band (600–1600 kHz). Data collection runs continuously for 14–19 h d⁻¹, centered on nighttime. Figure 1b shows the receiver with the attached cables and disk drive, and Fig. 1c is a block diagram of the receiving system.

Initial data processing is performed in real time on the Raspberry Pi. Achieving multiple narrow effective bandwidths for AM carrier detection from the input-continuous *I/Q* sample stream requires a very long (64 M) Fourier transform. To accomplish this task with limited computer memory, an 8192 × 8192 array implementation is used, which is a variation on those described extensively in the literature (e.g., Hocking, 1989; Ransom et al., 2002; and references therein). This implementation has the advantage not only of limiting memory requirement, but that the computation can be limited to the desired frequency resolution. In this case, approximately 100 8 Hz bands are used to bracket the frequencies of each AM signal, which in the US are licensed on 10 kHz spacings within the measured 1 MHz band. The resulting ∼100 power spectra have 0.016 Hz frequency resolution and a cadence of 33.5 s. Operation during 12–14 nighttime hours yields 160 MB of compressed data per day. From most sites, the data are transmitted daily to a master server at Dartmouth College, where custom software produces daily survey spectrograms displaying signal variation on selected AM stations. At sites with limited data transmission, software on the local Raspberry Pi produces the survey spectrograms, which are transmitted daily as compact PDF files. At those sites, locally stored data are periodically backed up to an external disk drive which is mailed to Dartmouth.

From April 2020 through March 2021, the hardware and software systems described above were deployed at six locations in the northeastern United States: Hanover, New Hampshire; New Bedford, Massachusetts; Ithaca, Schenectady, and Massena, New York; and Jenny Jump, New Jersey. Figure 2 shows a map of these locations, and Table 1 gives their exact latitudes and longitudes. The stations are arrayed around a targeted clear-channel and high-power (50 kW) AM radio transmitter, 810 kHz WGY in Schenectady, New York, indicated by a black star in Fig. 2. Under FCC license regulations, clear-channel AM radio stations are the only commercial transmission allowed in a given frequency range and in theory should not be subject to interference. Red squares in Fig. 2 show the nominal reflection locations of the signal paths of WGY to five of the receivers assuming one-hop propagation. The nominally measured reflection

Table 1. Locations of AM Doppler sounder receivers used in this study.

Receiver	Latitude (° N)	Longitude (° E)
Hanover, NH	43.705	−72.286
Schenectady, NY	42.813	−73.912
Jenny Jump, NJ	40.907	−74.925
New Bedford, MA	41.595	−70.910
Ithaca, NY	42.496	−76.431
Massena, NY	44.924	−74.898

points cover a clock-like pattern spanning an approximately 200 × 200 km area. Separation distances between transmitters and receivers must be kept within an optimal range to avoid dominance of ground waves at short baselines and dominance of multi-hop propagation at longer baselines. Receiver separations of ∼200 km in this experiment were motivated by the success of previous investigations (e.g., Chilcote et al., 2015). Some of the data shown below pertain to additional clear-channel AM stations: 1560 kHz WFME in New York City and 1080 kHz WTIC in Hartford, Connecticut, marked by blue and green stars, respectively. Blue and green triangles in Fig. 2 show the nominal reflection locations of the signal paths of WFME and WTIC to the six receivers, which cover a similar area of approximately 200 × 200 km each but are offset from that covered by the paths to the primary targeted AM station WGY. As pointed out by Chilcote et al. (2015), monitoring TIDs via Doppler sounding of clear-channel AM signals requires placing one receiver next to the target AM transmitter in order to record a reference signal, allowing separation of ionospheric Doppler shifts from variations in carrier frequency due to imperfect transmission equipment. In the present experiment, this is achieved with the receiver at Schenectady in the case of receiving WGY, the receiver at Jenny Jump in the case of receiving WTIC, and the receiver at New Bedford in the case of receiving WFME. In practice, only the WGY signal measured by the receiver in Schenectady required corrections to remove AM transmitter carrier drift.

3 Methodology

Figure 3 shows the reflected skywave from the 810 kHz WGY clear-channel station from each receiver from 21:00 to 12:00 UTC on the night of 26 September 2020. Evidence of a TID passing over the receiver array is apparent in the coherent variations in the signal attributed to the Doppler shift from 01:30 to 04:00 UTC (20:30–23:00 LT) on all six receivers. The signatures strongly resemble those reported by Chilcote et al. (2015) at 23:30–03:30 UTC (18:30–22:30 LT) on 12 April 2012, although the earlier measurement involved only three receivers.

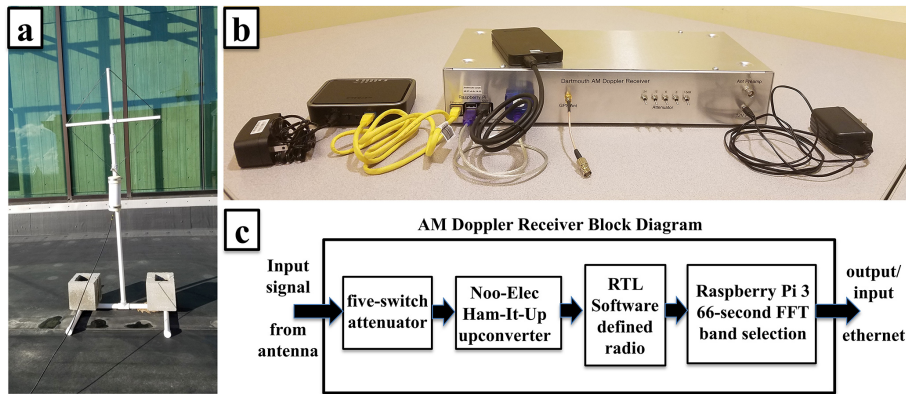


Figure 1. (a) The antenna/preamplifier used in the AM Doppler receiving systems, as deployed on the rooftop of an academic building; (b) the AM Doppler receiver with the associated cabling and external disk drive; (c) a block diagram of the receiver.

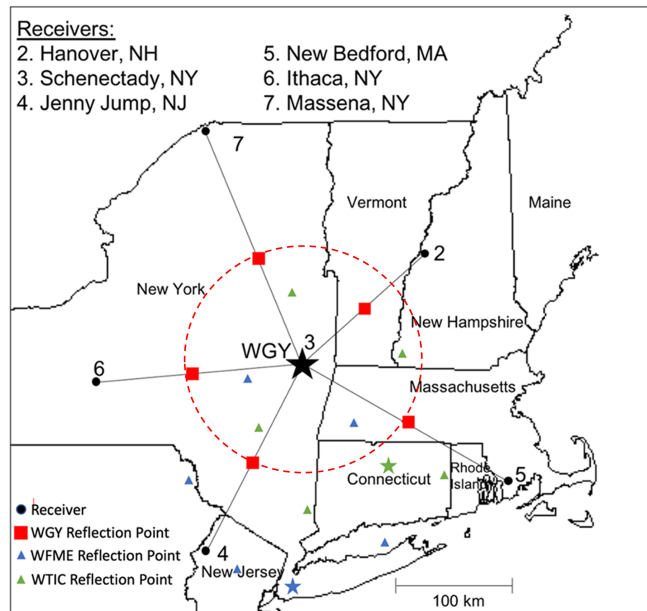


Figure 2. Map showing locations of transmitters (stars) and receivers (circles). Assuming specular, single-hop reflection places reflection points (squares and triangles) at the midway points. The network is designed for reception of the 810 kHz WGY clear-channel AM transmitter out of Schenectady, NY. The receivers encircle the WGY transmitter measuring the reflected wave in all directions over similar path lengths. Additional clear-channel signals at 1080 kHz (WTIC) and 1560 kHz (WFME) can be detected by the network, but reflected signals are measured over a limited angular extent across different path lengths.

The dashed red lines on each receiver in Fig. 3 trace the semi-automated tracking of the waveform used for analysis of TID characteristics. Semi-automated tracking software starts with a manual operation: through inspection of the frequency–time diagram, the user identifies times when the offset frequency of the carrier signal is clear and makes a

large excursion from its nominal frequency. The software then follows the signal backward and forward from these manually determined set points by identifying the frequency of the maximum signal in preceding or following time intervals, with the step size in time defined by the resolution of the measurement (30 s) and the step size in frequency capped to prevent the tracking from being discontinuous. Upon completion of this preliminary tracking, the software displays the determined preliminary track superposed on top of the spectrogram, allowing the user to identify intervals when the preliminary track diverges from the skywave. The software allows the user to insert time and frequency coordinates that override the automated determinations and update the tracking. Challenges to the automated tracking include the presence of a high-intensity ground wave (for example, see the New Bedford receiver at 04:00 UTC), multi-path conditions resulting in multiple Doppler-shifted signals at different frequencies (for example, see the Jenny Jump receiver at 03:00 UTC), and events when the signal is multi-valued and folds back on itself (third panel of Fig. 6 of Chilcote et al., 2015). The manual correction ensures a consistent carrier trace across all receivers.

A set of traces from a ring of receivers can be used to estimate the horizontal phase velocity of the TIDs detected by the system. The time delay of the variations in the Doppler-shifted signals between pairs of stations is the measured quantity used to determine the phase velocity. This time delay is determined using cross-correlation between each receiver's signal and the Hanover receiver's signal. A high correlation coefficient identifies maximum similarity between the signals. Using a sliding window, the cross-correlation function is executed across the entire domain of traced signals, and time intervals with stationary time delay and a high correlation coefficient are identified as intervals potentially containing TIDs. Stationarity, defined here as a stable delay that does not change with time for an extended period, typically on the order of 1 h, is required to ensure that the distur-

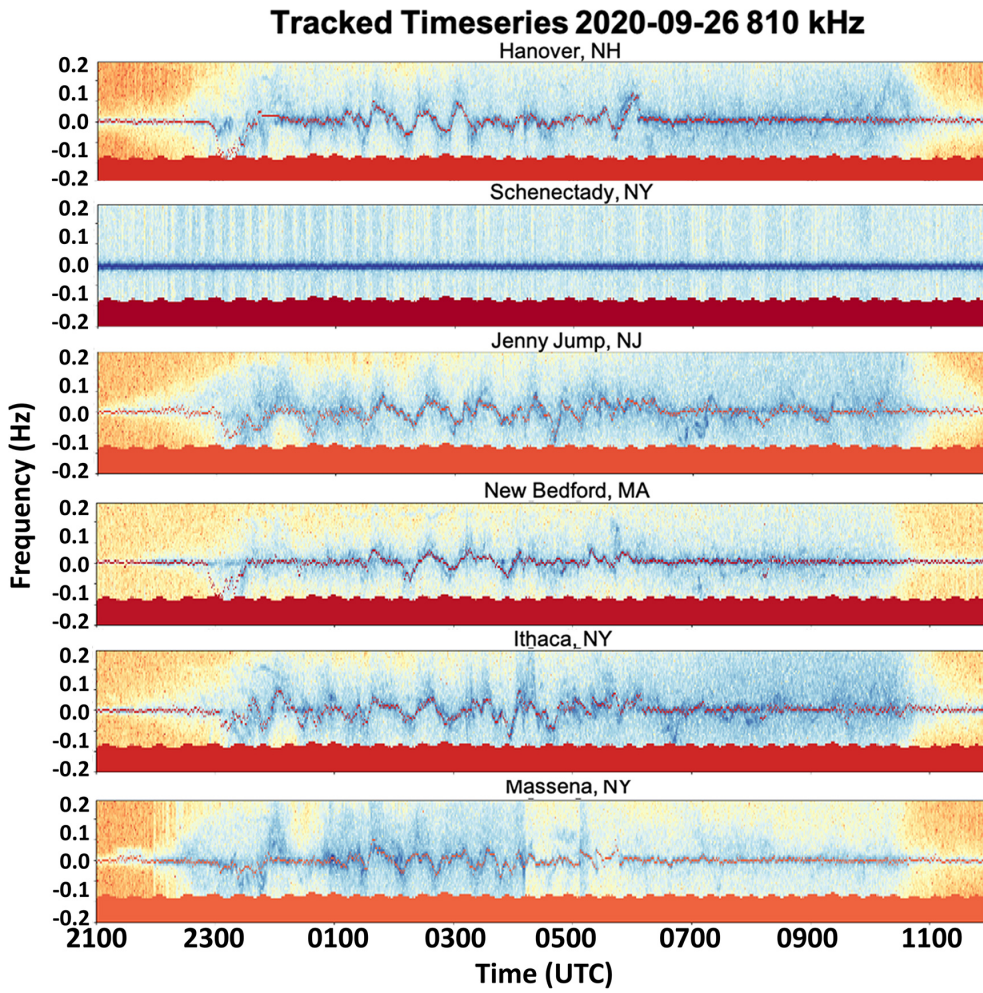


Figure 3. Spectrograms of the 810 kHz signal received at each location in the network covering 0.9 Hz bandwidth from 22:00 UTC on 25 September to 12:00 UTC on 26 September 2020. The solid, colored blocks at the base of each spectrogram illustrate the corrections made to account for variations in the frequency of the transmitted signal. The overlaid (red) trace is the extracted waveform generated by the semi-automated tracking algorithm with manual correction, as described in the text.

bance causing the Doppler shifts is consistent in shape and velocity across the entire array. Figure 4 shows the stationary, high-correlation time delays calculated with respect to the Hanover (light green) receiver for the event on the night of 26 September 2020 between 01:30 and 02:00 UTC. From the given time delays, it is immediately evident that the observed TID is propagating in the S/SE direction across the array as indicated by the red arrow.

We use three methods for determining the phase velocity from the time delays, denoted as triad, slowness, and sine fit. The triad method is a vector geometry approach to phase velocity which can be statistically analyzed because our experiment includes many baselines, i.e., many combinations of receiver triplets. A phase velocity can be calculated for each triplet as follows: for two pairs of receivers composing the triplet, the distance between reflection points is divided by the time delay between the received signals and inverted to

obtain vector components, and adding these vectors provides an estimate of inverse phase velocity pertinent to the triplet. This calculation is repeated for all possible combinations of three receivers and averaged to obtain a final estimate for the phase velocity:

$$V_{\text{phase}} = \frac{N}{\sum_{n=1}^{N!/(3!(N-3)!} \frac{1}{3} \cdot \left[\sum_{i=1}^3 \sum_{j=i+1}^3 \frac{\text{lag}_{ij} d_{ij}}{d_{ij}^2} \right]} \quad (1)$$

The “sine method” takes advantage of the arrangement of the reflection points, which lie approximately on a circle of radius $R = 100$ km centered on the Schenectady transmitter, indicated by a dashed line in Fig. 1. Using a Cartesian coordinate system with origin at Schenectady and with x directed eastward and y directed northward, this circle is described by $x^2 + y^2 = R^2$. Suppose a plane wave approaches this circle of receivers from the north, propagating in the $-y$ direction with velocity V . If the plane wave reaches the top of the cir-

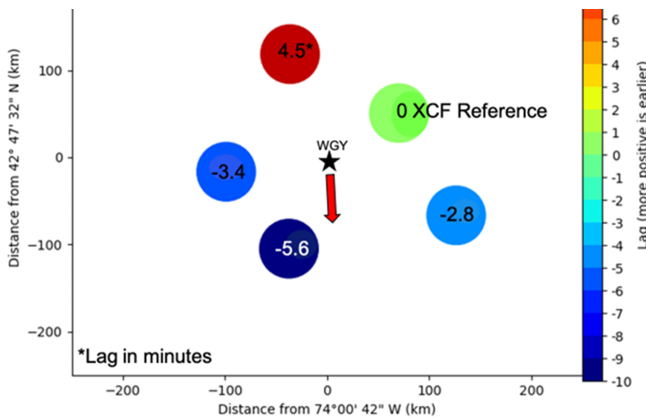


Figure 4. Map showing the location of each reflection point along with the time lag between frequency variations detected at each receiver and those detected at the Hanover, NH, receiver (arbitrarily chosen as reference) for the event detected at 02:00 UTC on 26 September 2020. Red indicates positive lags (signals arriving earlier), and blue indicates negative lags (signals arriving later). The observed lag times indicate a southern direction of propagation (arrow) for the observed TID.

cle ($x = 0, y = R$) at time $t = 0$, the equation for a wave front is $y = R - Vt$. Defining θ as the around-the-circle angle off of the y axis, x values of receivers around the circle are given by $x = R \sin \theta$. Inserting these x and y expressions into the equation for the circle and solving for t yields

$$t = (R/V)(1 - \cos \theta). \quad (2)$$

The time delay as a function of receiver position θ is therefore a sine wave; in this case, the receiver having minimum delay is that at $\theta = 0$ (at the northern edge of the circular array of receivers), and the receiver having maximum delay is that at $\theta = \pi$ (at the southern edge of the array). To treat plane waves coming in at other angles requires merely rotating the entire problem by the appropriate angle; for a plane wave directed at an angle φ off of the y axis, the time delay as a function of angular receiver position around the array would be

$$t = (R/V)(1 - \cos(\theta - \varphi)). \quad (3)$$

This function is fit to the measured delays of the five receivers arrayed at known angles θ around the origin (Schenectady) to determine the angle φ and the magnitude R/V , from which the direction of propagation and the horizontal phase velocity of the plane wave can be determined, since R is known.

The slowness method for tracking activity captured by a receiver array was originally developed in the seismology community (Lacross et al., 1969) and also applied to the location of thunder sources in storms (Johnson et al., 2011). Chum et al. (2014) and Chum and Podolska (2021) adapted this method for TIDs with a Doppler sounding array. As implemented with our array, the slowness parameter is defined

as the inverted phase velocity. Sampling a range of x and y components of the slowness generates an energy map, as defined by Chum et al. (2014), which is a measure of the alignment of the waveforms at the center of the array. The energy map, $W(s_x, s_y)$, is defined by

$$W(s_x, s_y) \propto \sum_{t_i=-\frac{\Delta t}{2}}^{\frac{\Delta t}{2}} \left[\frac{\sum_{n=1}^N f_{Dn}(t_i) + s_x \Delta x_n + s_y \Delta y_n + s_z \Delta z_n}{N} \right]^2 \quad (4)$$

and normalized according to

$$C(s_x, s_y) \propto \frac{W(s_x, s_y)}{\frac{1}{N} \times \sum_{n=1}^N \left[\sum_{t_i=-\frac{\Delta t}{2}}^{\frac{\Delta t}{2}} f_{Dn}(t_i)^2 \right]}, \quad (5)$$

where s_x and s_y are the x and y components of the slowness velocity and f_{Dn} is the Doppler shift measured at time t_i at the location of each reflection point. The Δx_i values in Eq. (4) are the distance from each reflection point to the center of the array. Since the array uses only the 810 kHz WGY signal for this study's analysis, the altitudes of reflection are assumed to be equal and the Δz term can be neglected. Figure 5 shows the energy map calculated using the slowness algorithm for 01:30–02:00 UTC on the night of 26 September 2020. We define the peak of the energy map (black circle) as the top 97 % of values, called peak slowness correlation coefficients. The distance from the center of the map to the centroid of the peak slowness correlation coefficients is the estimate of the magnitude of the inverse phase velocity, and the azimuthal direction of that centroid relative to the center of the map is the estimate of the direction of propagation. The inverse phase velocities associated with the extreme points of the region of peak slowness correlation coefficients can be taken as estimates of the relative uncertainty in magnitude (based on the inner and outer extrema relative to the origin) and direction (based on the azimuthal extrema). These relative uncertainty values are useful in comparing one phase velocity to another calculated with the slowness method, but they bear no obvious relation to the absolute uncertainty of the measurement.

Table 2 lists the events detected between 4 February 2020 and 31 March 2021, using the Schenectady station (WGY, 810 kHz) as the transmitter. These events were initially identified by manual inspection of reflected skywave plots similar to those shown in Fig. 3. The semi-automated tracking described above was applied to them. Phase velocities for each event, calculated using each of the three methods, are shown in the table.

The triad and sine fit methods both depend on the time delays determined from the normalized cross-correlation, making them especially sensitive to tails/outliers in the distribution of those delay times. Furthermore, both of these methods, but especially the sine method, become significantly less

Table 2. List of events detected using WGY Schenectady (810 kHz).

Event date (yyyy-mm-dd): time	Slowness phase velocity magnitude (direction)	Triad method velocity magnitude (direction)	Sine method velocity magnitude (direction)	Number of receivers
2020-03-23: 04:00 UTC	$478_{-260}^{+2277} \text{ m s}^{-1}$ (S)	414 (SSE)	n/a	3
2020-05-06: 04:00 UTC	$673_{-373}^{+770} \text{ m s}^{-1}$ (SE)	361 (SE)	352 (SE)	4
2020-07-14: 05:30 UTC	$358_{-124}^{+88} \text{ m s}^{-1}$ (SSE)	305 (SE)	298 (SE)	5
2020-09-09: 04:00 UTC	$150_{-8}^{+26} \text{ m s}^{-1}$ (NW)	237 (N)	248 (NE)	5
2020-09-22: 05:00 UTC	$267_{-85}^{+126} \text{ m s}^{-1}$ (SE)	343 (SE)	n/a	4
2020-09-26: 02:00 UTC	$538_{-244}^{+218} \text{ m s}^{-1}$ (S)	428 (S)	n/a	5
2020-09-27: 04:00 UTC	$335_{-97}^{+66} \text{ m s}^{-1}$ (SE)	300 (SE)	304 (SE)	5
2020-09-29: 02:00 UTC	$859_{-425}^{+218} \text{ m s}^{-1}$ (SW)	1099 (S)	1026 (SSW)	5
2020-11-15: 07:30 UTC	$332_{-84}^{+107} \text{ m s}^{-1}$ (SW)	446 (W)	n/a	5
2020-12-10: 07:00 UTC	n/a	498 (SSW)	381 (SW)	5
2020-12-29: 07:00 UTC	$229_{-34}^{+119} \text{ m s}^{-1}$ (NW)	158 (W)	155 (WNW)	4
2020-12-30: 07:00 UTC	$418_{-155}^{+168} \text{ m s}^{-1}$ (SW)	225 (NW)	219 (NW)	5
2021-01-26: 02:30 UTC	$299_{-112}^{+192} \text{ m s}^{-1}$ (S)	313 (SE)	270 (SE)	5

n/a: not applicable.

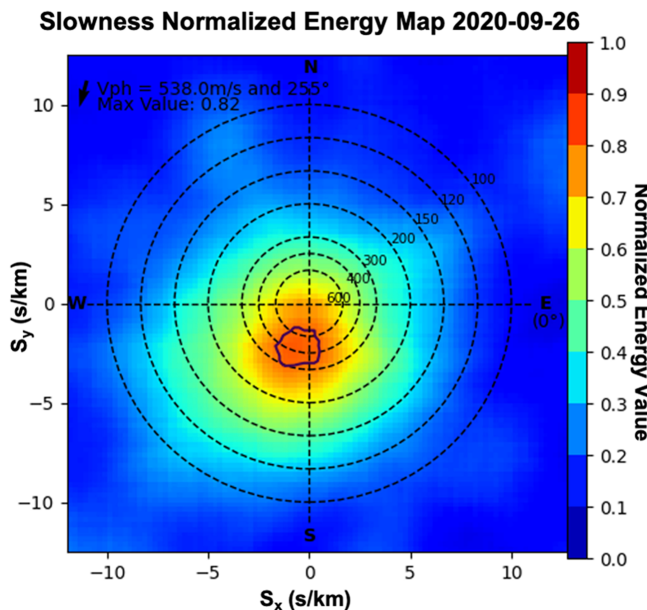


Figure 5. The slowness phase velocity energy map for the event occurring at 02:00 UTC on 26 September 2020. The region outlined with a solid trace indicates the peak region (top 3 % of slowness correlation coefficients). The phase velocity magnitude is calculated from a weighted centroid of the energy values within the peak region, and the angle to that centroid indicates the direction of propagation.

effective if fewer than five receivers are available. For these reasons, the slowness method, potentially combined with the normalized sliding cross-correlation for a consistency check, has the best potential for automation and scaling up these methods for tracking TIDs with large numbers of receivers. Velocities determined from the sine and triad method methods generally agree with those from the slowness method to within 45° with one (triad) to two (sine) outliers within 90° for the direction of propagation. The triad has a median of 343 m s^{-1} , a mean of 394 m s^{-1} , and a standard deviation of 232 m s^{-1} . The sine has a median of 298 m s^{-1} , a mean of 361 m s^{-1} , and a standard deviation of 258 m s^{-1} but was only functional when all five receivers were operational (9 out of 13 events).

Focusing on the slowness method results in Table 2, there are seven TIDs detected traveling in the S/SE direction, three events in the SW direction, and two events in the NW direction. For the event on 10 December 2020, the slowness method indicates an infinite phase velocity (i.e., the peak correlation coefficients region encircles the origin), although the sine and triad methods imply a southwesterly direction. Of the 13 events, 4 have phase velocities between 100 and 300 m s^{-1} , 3 have phase velocities between 300 and 400 m s^{-1} , 2 have phase velocities between 400 and 500 m s^{-1} , and 4 have phase velocities above 500 m s^{-1} . Larger phase velocities are accompanied by greater uncertainty. The four events below 300 m s^{-1} are likely classifiable as MSTIDs, while the remaining eight events above 300 m s^{-1} are likely LSTIDs. The median ve-

locity is 347 m s^{-1} , the mean velocity is 411 m s^{-1} , and the standard deviation is 199 m s^{-1} . For reference, the principal TID event analyzed by Chilcote et al. (2015) has a phase velocity of 330 m s^{-1} propagating in the northeast direction.

Assessing the possibility that E-region reflections might affect the results in Table 2 motivates the examination of vertical ionograms at 7.5 min cadence from mid-latitude observations at Westford, MA (42.6° N , 288.5° E). The ionosonde data, comprising station MHJ45 within the Global Ionosphere Radio Observatory (GIRO), originated from the University of Massachusetts Lowell's ionosonde station operated on the MIT Haystack observatory grounds. MHJ45 was located on the eastern edge of the study region. No sporadic E was recorded during any of the TID events in Tables 2–3 of our paper. Around event times, sporadic E was detected about 1 h before one of the events (on 26 September 2020), and an extremely weak Sporadic E layer was detected at 2 MHz frequency for 90 min after one of the events (30 December 2020). Based on this survey, the results in Table 2 are not significantly impacted by sporadic E propagation.

4 Validation with GNSS technique

For validation beyond the AM network observations, detected TID events can be compared with simultaneous observations of TID characteristics obtained from global navigation satellite system (GNSS) total electron content (TEC) data. TEC is the integrated electron density along a path between a ground receiver and a satellite. Time delays between different frequencies along the same path allow TEC to be calculated (Cooper et al., 2019). The measured TEC quantity is then projected geometrically onto the vertical axis and detrended from the baseline electron content. Detrended TEC as a function of time and space can show periodic increases and decreases which are linked to TID activity (Tsugawa et al., 2007; Zhang et al., 2022). The TEC technique and the AM Doppler sounding technique have different sensitivities in wave altitude and wave characteristics.

The detrended TEC (or differential TEC, dTEC) data, plotted in keogram form, are generated using global GNSS observations processed by MIT Haystack Observatory as part of operations for the Millstone Hill Geospace Facility (e.g., Zhang et al., 2017, 2019). In this analysis, 30 and 60 min sliding windows are used to determine the baseline electron content. The resulting keograms are analogous to slit cameras. A range of latitudes or longitudes (y axis) is chosen, and the dTEC for that narrow range is calculated and plotted for a number of hours (x axis). The TIDs become visible on the keograms as coherent regions of periodic increases and decreases in TEC which advance along the diagonal (changing latitude or longitude with time). GNSS data have been analyzed for the time intervals of the TIDs detected by the AM Doppler receivers (listed in Table 2). Figure 6 shows the 35 to 55° N keogram along the selected slit from -75

to -70° E , for the TID event on 26 September 2020, using a 30 min detrending window. From the angle of the coherent wave structure, the calculated phase velocity propagated southward at 430 m s^{-1} around 02:00 UTC. This phase velocity from GNSS TEC agrees well in magnitude and direction with that determined by the AM Doppler receiver network on the same date and time (see Table 2).

Table 3 presents results of comparing horizontal phase velocities of each event identified by AM Doppler sounding, estimated by the slowness method (second column) and estimated from simultaneous keograms from GNSS TEC data using two different detrending windows: 30 min (third column) and 60 min (fourth column). In 7 of 12 events for which an estimate is possible using both detrending windows, there is a significant difference between the magnitudes of the phase velocities inferred from the GNSS TEC data; in five of these cases, the value estimated with the 60 min detrend window agrees better with that inferred from the AM Doppler method, and, in two cases, the value estimated with the 30 min detrending window agrees better.

In all but three cases for which a coherent TID signature was observed in the GNSS TEC data, the directions of propagation determined from at least one of the GNSS TEC calculations is within 45° of those determined from the AM Doppler receiver network/slowness analysis. One exception occurs on 26 January 2021 when a 90° discrepancy is observed. The other exceptions are 180° discrepancies occurring on 30 December and 22 September 2020; in the first case, for the GNSS TEC estimate, only the 30 min detrend window gives a result, and, in the second case, the triad and sine methods give a direction opposite to that of the slowness method and in agreement with the GNSS TEC estimate. For the event on 26 January 2021, the AM Doppler system detects a TID which propagates southward with a phase velocity of 219 m s^{-1} and has been linked to an auroral source (see Sect. 5), and the TEC keogram detects an event propagating westward with a phase velocity of 130 m s^{-1} . It is likely in this case that the two techniques detect two distinct TIDs: one caused by an auroral event and prominent at lower altitudes and one potentially caused by the electrodynamically driven Perkins instability (Perkins, 1973; Narayanan et al., 2018). The configuration is suggested by the TID's direction of propagation and phase speed which would have more prominent effect at the higher altitudes to which the GNSS TEC technique is more sensitive.

Concerning magnitudes of the horizontal phase velocities, there is somewhat less concordance between AM Doppler and GNSS-based estimates. In 7 of 12 cases, the magnitudes agree to within 150 m s^{-1} (ranging from 15 to 136 m s^{-1}), although, in one of these cases, the direction differs by 90° . In 5 of 12 cases, the magnitudes disagree by more than 150 m s^{-1} (ranging from 157 to 366 m s^{-1}). In one of these cases, the directions agree, but, in the others, the directions disagree by 90° or more. In the four cases for which the GNSS TEC method indicates only a meridional or zonal

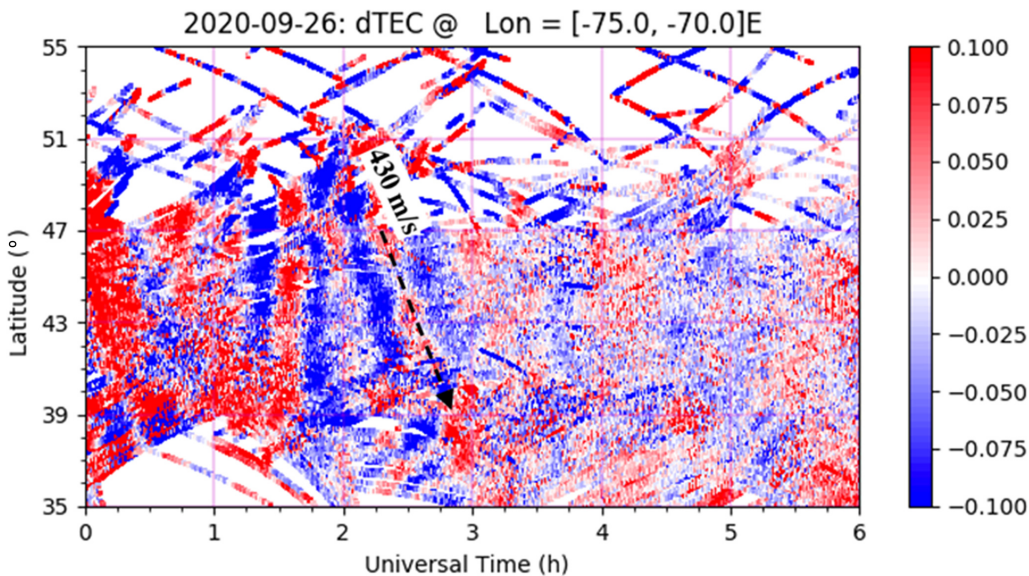


Figure 6. Differential TEC keogram for a TID detected via GNSS on the night of 26 September 2020, using a 30 min detrending window. The keogram indicates a coherent structure propagating southward with a phase velocity of 430 m s^{-1} . The keogram corroborates the TID event direction and speed measured with the AM Doppler receiving network at the same time.

component, three of these are within 20 % of the phase velocities determined from the AM Doppler receiver network/slowness analysis. For the other five events, the GNSS TEC method indicates both meridional and zonal components. Since phase velocities must be inverted to be added, the smaller-amplitude component becomes the dominant phase velocity. In these five cases, the slowness-calculated phase velocity is larger than that inferred from the GNSS TEC method. In fact, out of the 11 events for which the directions agree between the two techniques, 9 had slowness phase velocities greater than their TEC counterparts.

A possible explanation for this observed discrepancy is that the GNSS TEC method, relying on an integral of electron density through the ionosphere, is most sensitive in general to the peak electron density regions at higher F2 altitudes in the ionosphere, while the AM Doppler sounding technique exclusively looks at reflection off the bottom of the ionosphere. Since a TID has a vertical wavenumber, its characteristics are altitude-dependent. The Doppler sounding technique is only able to determine information about the horizontal wavenumber, but contributions from the vertical may be sufficient to explain the discrepancy in magnitude between the two techniques. Another potential factor to consider is the detrending technique employed in GNSS TID analysis, which may lead to the detection of only specific components of multifrequency waves. In the context of the 30 and 60 min sliding windows used in this study, larger-scale and longer-periodicity waves tend to be attenuated. Table 3 appears to indicate that these GNSS-TEC-derived TID phase speeds are indeed slower; therefore these waves likely contain some MSTID components.

In aggregate, the TEC and AM Doppler observations show that the TID wave environment is sometimes complex, with multiple waves of different characteristics simultaneously present and detected favorably by one technique or the other. The consistency of the two techniques for both magnitude and direction of the horizontal phase velocity for a slight majority of the observed events in this work suggests that they often observe the same TIDs. However, the occurrence of discrepancies almost half the time, including cases in which the two methods give opposite directions, suggests that the unexplained discrepancy between directions of propagation previously seen in Chilcote et al. (2015) was not uncommon and results from a complex wave environment, similar to the 15 November 2020 and 26 January 2021 events in this study. Possibly, a contributing factor was additional error in the AM Doppler technique introduced by their experimental setup, which relied on multiple frequencies from different radio transmitters and only used three receivers.

5 Connections to auroral activity

Auroral geomagnetic storms and substorms can enhance the auroral electrojet, which then initiates TIDs through Lorentz forces and Joule heating (Ding et al., 2008). To detect the occurrence of this mechanism, electrojet enhancements can be tracked through the Auroral Electrojet (AE) index (Davis and Sugiura, 1966) and spatially and temporally isolated using magnetometer data from instruments maintained in several arrays of arctic observatories, such as the Canadian Array for Realtime Investigations of Magnetic Activity (CARISMA), the Canadian High Arctic Ionospheric Network (CHAIN),

Table 3. Comparisons of TID events detected with both AM Doppler sounding and GNSS.

Event date (yyyy-mm-dd): time	Slowness phase velocity magnitude (direction)	GNSS TEC phase velocity, 30 min detrend magnitude (direction)	GNSS TEC phase velocity, 60 min detrend magnitude (direction)	Kp index
2020-03-23: 04:00 UTC	478 m s ⁻¹ (S)	485 m s ⁻¹ (S)	517 m s ⁻¹ (S)	3+
2020-05-06: 04:00 UTC	673 m s ⁻¹ (SE)	320 m s ⁻¹ (S) and 190 m s ⁻¹ (E) = 163 m s ⁻¹	537 m s ⁻¹ (S)	2+
2020-07-14: 05:30 UTC	358 m s ⁻¹ (SSE)	645 m s ⁻¹ (S) and 165 m s ⁻¹ (E) = 160 m s ⁻¹	645 m s ⁻¹ (S) and 384 m s ⁻¹ (W) = 330 m s ⁻¹	4–
2020-09-09: 04:00 UTC	150 m s ⁻¹ (NW)	170 m s ⁻¹ (N) 150 m s ⁻¹ (W) = 113 m s ⁻¹	129 m s ⁻¹ (N) and 160 m s ⁻¹ (W) = 101 m s ⁻¹	0
2020-09-22: 05:00 UTC	267 m s ⁻¹ (SE)	154 m s ⁻¹ (N) 155 m s ⁻¹ (W) = 109 m s ⁻¹	No pattern observed	3–
2020-09-26: 02:00 UTC	538 m s ⁻¹ (S)	430 m s ⁻¹ (S)	445 m s ⁻¹ (S)	4
2020-09-27: 04:00 UTC	335 m s ⁻¹ (SE)	140 m s ⁻¹ (W) (well defined), 115 m s ⁻¹ (S) (faint)	320 m s ⁻¹ (S)	4
2020-09-29: 02:00 UTC	859 m s ⁻¹ (SW)	580 m s ⁻¹ (S); 645 m s ⁻¹ (S) = 430 m s ⁻¹	780 m s ⁻¹ (S)	4
2020-11-15: 07:30 UTC	332 m s ⁻¹ (SW)	130 m s ⁻¹ (N); 165 m s ⁻¹ (W) = 102 m s ⁻¹	85 m s ⁻¹ (S) and 60 m s ⁻¹ (W) = 50 m s ⁻¹	0
2020-12-10: 07:00 UTC	n/a	80 m s ⁻¹ (S) and 60 m s ⁻¹ (W) (multiple wavefronts)	103 m s ⁻¹ (N) and 60 m s ⁻¹ (W) = 55 m s ⁻¹	1
2020-12-29: 07:00 UTC	229 m s ⁻¹ (NW)	215 m s ⁻¹ (S) and 60 m s ⁻¹ (W) = 58 m s ⁻¹ , also weak northward	129 m s ⁻¹ (N) and 60 m s ⁻¹ (W) = 55 m s ⁻¹	1–
2020-12-30: 07:00 UTC	418 m s ⁻¹ (SW)	145 m s ⁻¹ (N) and 80 m s ⁻¹ (W) = 70 m s ⁻¹ (multiple wavefronts)	107 m s ⁻¹ (N) and 60 m s ⁻¹ (W) = 52 m s ⁻¹	2–
2021-01-26: 02:30 UTC	299 m s ⁻¹ (S)	130 m s ⁻¹ (W) (multiple waves)	120 m s ⁻¹ (W)	4–

n/a: not applicable.

and the Time History of Events and Macroscale Interactions during Substorms (THEMIS) ground array. Enhancement events can then be correlated with southward-propagating TIDs measured across the AM Doppler sounding network in the northeastern United States.

Figure 7 shows the AE index for 00:00–12:00 UTC on 14 July 2020 and a map of magnetometer activity at 03:30 UTC on the same date. An enhancement in AE occurs at approximately 03:40 UTC, 1 h 50 min prior to a southeastward-propagating TID with a measured phase velocity of 358 m s⁻¹ on 14 July 2020 (Table 2). Assuming that the group and phase velocities are on the same order, the distance traveled by the TID over the 1 h 50 min between the AE enhancement and its arrival at the AM receiver network is approximately 2360 km. The distance from the epicenter of the magnetic activity (Churchill, Manitoba) to the center of our network (Schenectady, NY) is 2300 km, qualitatively

confirming the hypothesis that auroral activity and the southward TIDs are correlated in this case.

Of the 13 TID events listed in Table 2, 7 were associated with auroral activity indicated by enhanced AE indices; these occurred on 23 March, 6 May, 14 July, 26 September, 27 September, 29 September 2020, and 26 January 2021. For 4 of these, spatial and temporal correlations between the enhancements of the AE index and the detections of the TIDs, as described above and in Fig. 7, were consistent with an auroral cause for the observed TIDs; these occurred on 6 May, 14 July, 26 September, and 27 September 2020. No enhancement in AE index was noted in association with the other TID events in Table 1. The far-right column of Table 3 lists the 3 h Kp index at the time of each TID event. These vary widely from 0–4. Not surprisingly, the 7 events associated with auroral activity monitored by AE also correspond to the highest Kp values.

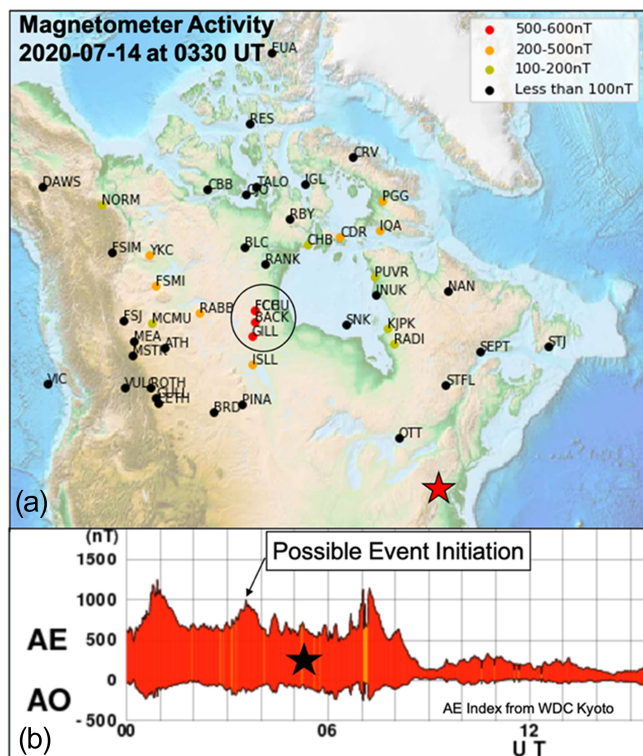


Figure 7. Magnetometer activity (a) at 03:30 UTC and the Auroral Electrojet (AE) index (b) for 00:00–15:00 UTC on 14 July 2020. The enhancement in the AE index at approximately 03:40 UTC corresponds to maximum magnetic activity, on the order of 500–600 nT magnitude, in the vicinity of Churchill, Manitoba. This activity precedes a TID event detected with the AM Doppler receiver network in the northeastern United States by 1 h 50 min, approximately matching the time it would take a TID with a measured phase velocity of 358 m s^{-1} to propagate from Churchill to the measurement array.

6 Fully automated detection and characterization of TIDs

The results of Sects. 3–5 are based on semi-automatic tracking of variations in Doppler shift on six receivers, supplemented by manual corrections. To enable an operational system that considers larger numbers of events and, more importantly, larger numbers of receivers monitoring larger numbers of clear-channel AM stations, it is essential to remove any manual actions and entirely automate event detection and characterization. To test the efficacy of purely automated analysis, a modified version of the tracking software described in Sect. 3 was applied to a 12-month data set with automated initial peak selection and no manual correction.

Using the resulting Doppler shift versus time on all six receivers tracked fully autonomously, slowness distribution functions were calculated for consecutive 55 min intervals between sunrise and sunset each day. Intervals for which the maximum slowness correlation value was above an experi-

mentally determined threshold, together with preceding and following intervals, were re-analyzed with higher effective time resolution to determine the interval of maximum correlation between the six receivers. The phase velocity and direction were calculated for these maximum correlation intervals. Events with multi-modal distribution functions or uncertainties too large in velocity magnitude or direction were discarded.

The auto-tracker method was applied to Doppler sounding data from all receiving sites for the three selected clear-channel AM transmitters for 359 d between 3 April 2020 and 31 March 2021. The selected stations were 810 kHz (WGY from Schenectady, New York), 1080 kHz (WTIC from Hartford, Connecticut), and 1560 kHz (WFME from New York City), as shown in Fig. 2. The 810 kHz station contained many false positives caused by erroneous slowness correlation coefficients due to the reduced amplitude of the Doppler signatures on WGY, as the lowest-frequency station. The false positives were mitigated with a threshold RMS value on the correlation, but event detection still required manual verification.

Figure 8 shows the results of the automated event detection. Each triplet of panels represents the set of events detected with a unique transmitting frequency: 810 kHz (top), 1080 kHz (middle), and 1560 kHz (bottom). Within each set, the top two panels show the events as a function of time of day and time of year. For the top two panels in each set, the color bar on the right indicates the magnitude of the phase velocity of each TID. In the second panel, arrows indicate the direction of propagation. In the bottom panel, events are binned by month in histogram format.

The method identified 18 TID events at 810 kHz (0.05 events per day), 25 events at 1080 kHz (0.07 events per day), and 46 events at 1560 kHz (0.14 events per day). Significantly, nearly 3 times the number of events are seen on the highest-frequency station compared to the lowest. Manual inspection of the Doppler spectrograms confirms that the variations in the skywave traces are much more distinct and that auto-tracking is more effective for transmitter frequencies $> 1 \text{ MHz}$, particularly the variations typical of TIDs. Figure 9 illustrates this difference for a typical TID event observed on 27 September 2020. The amplitude of the Doppler shift induced when the AM carrier reflects from a vertically moving ionospheric layer is proportional to the frequency of the signal:

$$\Delta f = -2f \times \frac{v}{c}, \quad (6)$$

where v is the vertical component of the velocity of the ionosphere, Δf is the frequency excursion, and f is the carrier frequency. Hence, for given TID parameters, the key measured quantity Δf is proportional to the frequency. Furthermore, higher frequencies reflect at higher altitudes where TIDs themselves have greater amplitudes due to energy conversion as the number of neutral particles decreases with al-

April 2020–March 2021 Automated Event Detection

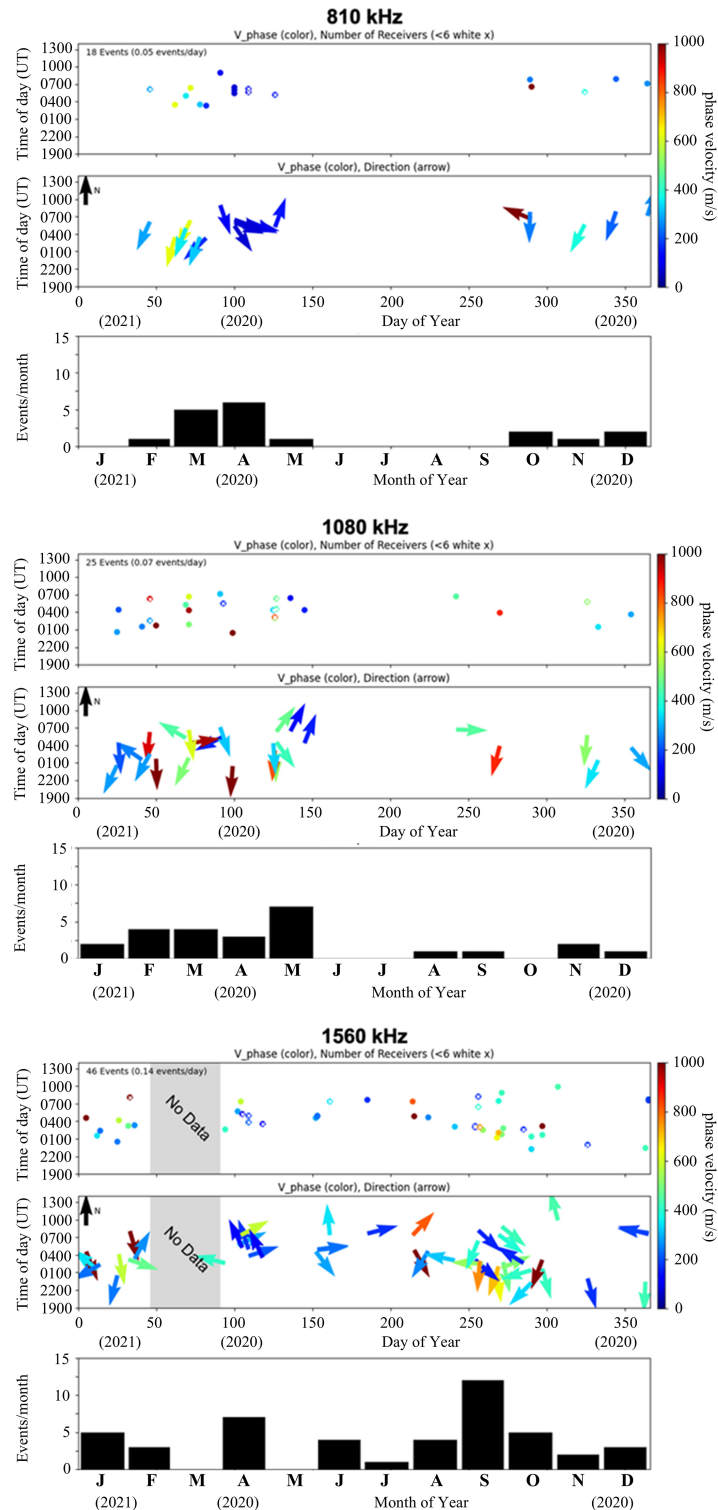


Figure 8. Results of the fully automated tracking and event detection software: each triplet of panels indicates automatically detected events from 810, 1080, and 1560 kHz AM stations, respectively. The top panel of each triplet displays the phase velocity (color) as a function of day of year (x axis) and time of day (y axis). The second panel displays the direction of propagation for each event, and the lowest panel groups the detected events by month. Seasonal dependence of maximal event detection suggests the automated tracking favors the detection of LSTIDs (see text discussion). Day of year runs from 1–366, although January–March pertains to 2021 and April–December pertains to 2020.

titude (Houghton, 2002). In addition to reduced amplitudes, at lower frequencies it is more common that the radius curvature of the wave is smaller than the mean height. In these cases, multiple reflections can occur for the same frequency, and this generates S-shaped features that fold back on themselves (Fiser et al., 2017). Given that the same ionospheric velocities produce larger absolute deviations from the carrier frequency and are less likely to exhibit anomalous features, it is therefore not surprising, as Fig. 8 confirms, that the AM Doppler technique for detecting TIDs is much more effective if applied to AM signals in the upper half of the AM frequency band > 1 MHz.

7 Seasonal dependence of AM-network-identified TIDs and comments on technique optimization

Seasonal dependence of TID events identified with the AM Doppler method is shown in the histogram panels of Fig. 8. For all three frequencies, there is a distinct minimum occurrence in the summer (days 150–215) and hints of equinoctial peaks. The summer minimum in occurrence rate is clearly inconsistent with previous studies of nighttime mid-latitude MSTIDs using a variety of techniques. For example, optical imager data recorded at Haleakala from 2006–2012 show winter and summer peaks in occurrence rate of MSTIDs with minima around the equinoxes (Fig. 3 of Duly et al., 2013). Analysis of 2 years of optical imager data from two locations in Japan (Fig. 4b of Shiokawa et al., 2003) and 4 years of data at Arecibo (Fig. 2 of Martinis et al., 2010) also show winter and summer peaks in occurrence rate. A different technique, GNSS observations from an array of observatories in Europe, shows a winter peak and a weak secondary summer peak in occurrence rate of nighttime MSTIDs in the mid-latitude ($< 55^\circ$) portion of the array (Fig. 3 of Otsuka et al., 2013). Another GNSS study with a more global array also finds that the nighttime MSTID occurrence rate peaks in summer in many longitude sectors (Fig. 5 of Kotake et al., 2006). Yet another technique, in situ satellite measurements of F-region plasma density undulations which may be associated with MSTIDs, also reveals equinoctial minima and summer or winter maxima in occurrence rates of nighttime mid-latitude undulations (Figs. 2–4 of Park et al., 2010). Other optical imager studies of mid-latitude nighttime MSTIDs show winter peaks in occurrence rate but are inconclusive about summer (Garcia et al., 2000) or show weakest events in fall and more intense ones in winter and summer (Tsuboi et al., 2023). The preponderance of all of these previous studies demonstrates that the seasonal dependence found in Fig. 8 is not consistent with mid-latitude nighttime MSTIDs.

Possibly the observed seasonal dependence of TIDs measured with the AM Doppler technique is more consistent with mid-latitude nighttime LSTIDs. For example, Tsugawa et al. (2004) observed peaks in LSTID occurrence around the equinoxes in the spring and fall, absence of quiet-time

Event Frequency Signature Comparison: 2020-09-27

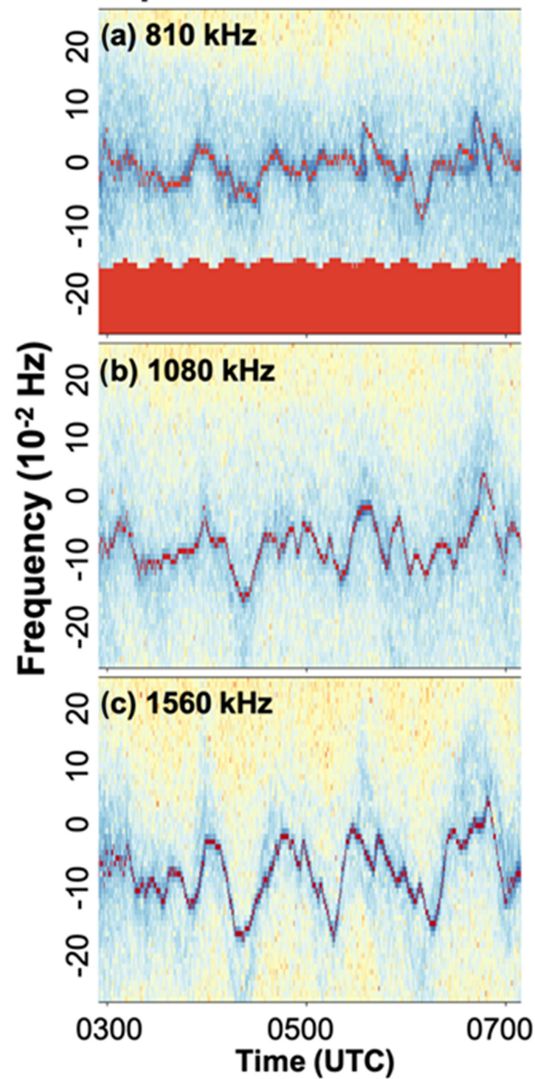


Figure 9. Spectrograms of the 810, 1080, and 1560 kHz signals, covering 0.9 Hz bandwidth for 03:00–07:00 UTC on 27 September 2020. As expected from Eq. (4), the Doppler shift is a function of the frequency (larger for higher frequencies). The figure indicates that TIDs may be easier to detect and track using carriers in the upper half of the AM band.

LSTIDs in summer, and minimum occurrence of LSTIDs in summer during active geomagnetic periods. Yakovets et al. (2011) and Ding et al. (2014) detected similar activity peaks at the equinoxes for LSTIDs. Because seasonal statistics of TID characteristics may depend on local time and region, it is difficult to draw firm conclusions, but the seasonal dependence seen in Fig. 8 suggests that the automated tracking and event detection algorithm employed here may preferentially detect LSTIDs, perhaps because their larger wavelengths imply that the resulting Doppler shift variations

have longer timescales and are easier to track. Another possibility is that the fully automated AM Doppler technique is sensitive to both MSTIDs and LSTIDs but that the method is significantly less sensitive in summer, perhaps due to different ionospheric conditions. Detailed interpretation of the seasonal dependence of TIDs detected by the novel fully automated AM Doppler method requires further study of larger data sets.

For all three transmitter frequencies, the detected TIDs primarily propagate southward. Southward components to the phase velocity are observed for 15 of 18 events on 810 kHz, 19 of 25 on 1080 kHz, and 28 of 46 on 1560 kHz. The east-west propagation is split almost equally in all three data sets: 9 out of 18 westward on 810 kHz, 12 out of 25 westward on 1080 kHz, and 22 out of 46 westward on 1560 kHz. On the 810 kHz station, the phase velocities range from 71 to 1308 m s^{-1} with a mean phase velocity of 304 m s^{-1} and a standard deviation of 295 m s^{-1} . On the 1080 kHz station, the phase velocities range from 130 to 1453 m s^{-1} with a mean phase velocity of 515 m s^{-1} and a standard deviation of 329 m s^{-1} . On the 1560 kHz station, the phase velocities range from 104 to 1914 m s^{-1} with a mean phase velocity of 445 m s^{-1} and a standard deviation of 367 m s^{-1} .

Of the 13 events identified for analysis by the manual methods, 7 of those events are detected by the auto-tracker on at least one transmitter frequency. The auto-tracker initially detects an additional 2 of the 13 manually detected events, but these 2 fail to meet the auto-tracker's criteria on the uncertainty in phase velocity magnitude or direction. The imperfect overlap between the manually selected events and those detected with the auto-tracker technique may be attributed to the preferential detection of LSTIDs, the fact that the automated system performs less optimally on the 810 kHz, and the discrepancies that exist between the two frequencies with purely human-in-the-loop detection and tracking.

To investigate discrepancies between the 1560 and the 810 kHz results, the semi-automated analysis described in Sect. 3 was applied to the 1560 kHz data set for the 13 TID events for which a similar analysis applied to the 810 kHz data set is summarized in Table 2. In 8 out of the 10 events for which comparison was possible, the direction of propagation of the detected TIDs on the 810 vs. 1560 kHz matches within 45° , but the magnitude of the phase velocity on the 1560 kHz station is generally greater than that measured on the 810 kHz station. This discrepancy could be introduced by different reflection heights between the two frequencies; alternatively, it could be due to error introduced because the receivers do not encircle the 1560 kHz station. Therefore, the received signals may be from oblique reflections off the ionosphere, may have different reflection path lengths, and/or may sample a smaller angular spread of the ionosphere. For optimal system designs, receivers should encircle the transmitters equidistant from primary transmitters.

Ultimately, the results of Fig. 8 demonstrate the feasibility of automatic TID detection applied to spectral data of Doppler shifts of multiple receiver clear-channel AM signals at multiple receiver locations. The results also indicate this technique is far more effective when applied to signals in the upper part of the AM band. For such signals, the detection software used here has identified approximately one event per week, and seasonal statistics suggest the LSTIDs are favored over MSTIDs. Further refinement of the algorithm could result in sensitivity to more events and greater sensitivity to MSTIDs. The automatic event detection demonstrated herein is essential if the technique is to be practical using configurations with large numbers of AM signals measured at a large number of receiving stations.

8 Conclusions

This study has demonstrated the efficacy of using a circular network of AM receivers around a single transmitting frequency to identify TIDs and their characteristics from Doppler-shifted reflected skywaves. While Chilcote et al. (2015) showed that TIDs can be detected via Doppler sounding using AM signals, their use of only three receivers and a number of different frequencies for a single detected TID did not establish that TID horizontal phase velocity magnitude and direction could be reliably corroborated by other methods, namely GNSS TEC observations. However, a larger sample set with a more robust measurement design from the present study has shown good agreement between horizontal phase velocities determined from GNSS TEC data and those derived from AM Doppler sounding in slightly more than half of the events studied, suggesting that these techniques often observe the same TIDs. Differences between the horizontal phase velocities inferred from two data sets in somewhat less than half the cases can be attributed to the different sensitivities of the two measurement techniques in a complex TID wave environment. In this context, it is not surprising that the one example previously studied by Chilcote et al. (2015) showed a significant discrepancy between phase velocities inferred from the two techniques. Most detected TIDs had a southward phase velocity, and, in four cases, they were associated with enhanced auroral magnetic activity which may have been their source, based on timing, location, and TID velocity.

This experiment, particularly successful implementation of purely automated analysis, clearly indicates that it is possible to extend AM Doppler sounding to large numbers of receivers. Based on these results, a future experiment could be envisioned using a few dozen receivers arrayed around a dozen or more clear-channel AM transmitters to achieve continental-scale spatial coverage, allowing TIDs to be tracked for $\sim 1000 \text{ km}$ or more. Such an array would effectively complement spatial coverage of the GNSS technique, allowing differences and similarities be-

tween the two techniques to be better understood, to the improvement of both. An array covering a continental or half-continental scale would also supplement existing optical, digisonde, and SuperDARN radar techniques, further leveraging investments and science yield from those already productive assets. We suggest that future AM Doppler network experiments should employ transmitters in the upper part of the AM band for best results. Additional refinement of the purely automated algorithm may lead to greater sensitivity and more event detections.

Data availability. Data used in this study are available at <https://doi.org/10.7910/DVN/L3JXIH> through LaBelle (2024).

Author contributions. CCT performed most of the data analysis and wrote the initial draft of the article with contributions from the other co-authors. JL participated in deploying the instruments, data acquisition, data analysis, and article preparation. PJE participated in deploying instruments to the Schenectady site, data analysis, and article preparation. SRZ participated in data analysis and article preparation. DM participated in development, construction, and deployment of the radio receiving systems and consulted on data analysis and article preparation. TK participated in development and maintenance of software for acquisition and archiving of the radio data.

Competing interests. The contact author has declared that none of the authors has any competing interests.

Disclaimer. Publisher's note: Copernicus Publications remains neutral with regard to jurisdictional claims made in the text, published maps, institutional affiliations, or any other geographical representation in this paper. While Copernicus Publications makes every effort to include appropriate place names, the final responsibility lies with the authors.

Acknowledgements. The work at Dartmouth College was supported by the National Science Foundation (grant no. AGS-1915058). Total electron content data were provided to the community through Millstone Hill Geospace Facility operations at MIT Haystack Observatory under National Science Foundation grant no. AGS-1952737 to the Massachusetts Institute of Technology. Shun-Rong Zhang acknowledge NSF award no. AGS-2149698 and NASA grant no. 80NSSC21K1310. The authors thank the many Dartmouth undergraduate students who contributed to various stages of this project, including Rongfei Lu, Jeffrey Kim, Eric Tao, Eldred Lee, Nathan Grice, and Carter Person. The authors acknowledge the citizen science contributions of the late John S. Erickson, who provided internet and station infrastructure to this project at his Schenectady, NY, residence for the crucial WGY reference clear-channel station recording.

Financial support. This research has been supported by the National Science Foundation (grant nos. AGS-1915058, AGS-1952737, and AGS-2149698) and the National Aeronautics and Space Administration (grant no. 80NSSC21K1310).

Review statement. This paper was edited by Jorge Luis Chau and reviewed by Mani Sivakandan and Stephen Kaepller.

References

Beley, V. S., Galushko, V. G., and Yampolski, Y. M.: Traveling ionospheric disturbance diagnostics using HF signal trajectory parameter variations, *Radio Sci.*, 30, 1739–1752, 1995.

Chan, K. L. and Villard, O. G.: Observation of large-scale traveling ionospheric disturbances by spaced-path high-frequency instantaneous-frequency measurements, *J. Geophys. Res.*, 67, 973–988, 1962.

Chilcote, M., LaBelle, J., Lind, F. D., Coster, A. J., Miller, E. S., Galkin, I. A., and Weatherwax, A. T.: Detection of traveling ionospheric disturbances by medium-frequency Doppler sounding using AM radio transmissions, *Radio Sci.*, 50, 249–263, 2015.

Chum, J., F. Bonomi, A. M., Fišer, J., Cabrera, M. A., Ezquer, R. G., Burešová, and D., Laštovička, J.: Propagation of gravity waves and spread F in the low-latitude ionosphere over Tucumán, Argentina, by continuous Doppler sounding: First results, *J. Geophys. Res.-Space*, 119, 6954–6965, 2014.

Chum, J. and Podolska, K.: 3D Analysis of GW Propagation in the Ionosphere, *Geophys. Res. Lett.*, 45, 11562–11571, 2021.

Cooper, C., Mitchell, C. N., Wright, C. J., Jackson, D. R., and Witvliet, B. A.: Measurement of ionospheric total electron content using single-frequency geostationary satellite observations, *Radio Sci.*, 54, 10–19, 2019.

Cosgrove, R. B.: Generation of mesoscale F layer structure and electric fields by the combined Perkins and E_s layer instabilities, in simulations, *Ann. Geophys.*, 25, 1579–1601, <https://doi.org/10.5194/angeo-25-1579-2007>, 2007.

Cosgrove, R. B. and Tsunoda, R. T.: A direction-dependent instability of sporadic-E layers in the nighttime mid-latitudes ionosphere, *Geophys. Res. Lett.*, 29, 1864, <https://doi.org/10.1029/2002GL014669>, 2002.

Cosgrove, R. B. and Tsunoda, R. T.: Instability of the E-F coupled nighttime midlatitude ionosphere, *J. Geophys. Res.-Space*, 109, A04305, <https://doi.org/10.1029/2003JA010243>, 2004.

Davies, K.: A measurement of ionospheric drifts by means of a Doppler shift technique, *J. Geophys. Res.*, 67, 4909–4913, 1962.

Davis, T. N. and Sugiura, M.: Auroral electrojet activity index AE and its universal time variations, *J. Geophys. Res.*, 71, 785–801, 1966.

Ding, F., Wan, W., Liu, L., Afraimovich, E. L., Voeykov, S. V., and Perevalova, N. P.: A statistical study of large-scale traveling ionospheric disturbances observed by GPS TEC during major magnetic storms over the years 2003–2005, *J. Geophys. Res.-Space*, 113, A00A01, <https://doi.org/10.1029/2008JA013037>, 2008.

Ding, F., Wan, W., Li, Q., Zhang, R., Song, Q., Ning, B., Liu, L., Zhao, B., and Xiong, B.: Comparative climatological study of large-scale traveling ionospheric disturbances over North Amer-

ica and China in 2011–2012, *J. Geophys. Res.-Space*, 119, 519–529, 2014.

Duly, T. M., Chapagain, N. P., and Makela, J. J.: Climatology of nighttime medium-scale traveling ionospheric disturbances (MSTIDs) in the Central Pacific and South American sectors, *Ann. Geophys.*, 31, 2229–2237, <https://doi.org/10.5194/angeo-31-2229-2013>, 2013.

Essen, L.: International frequency comparisons by means of standard radio frequency emissions, *P. Roy. Soc. Lon. Ser. A*, 149, 506–510, 1935.

Fenwick, R. C. and Villard, O. G.: Continuous recordings of the frequency variation of the WWV-20 signal after propagation over a 4000-km path, *J. Geophys. Res.*, 65, 3249–3260, 1960.

Fišer, J., Chum, J., and Liu, J.-Y.: Medium-scale traveling ionospheric disturbances over Taiwan observed with HF Doppler sounding, *Earth Planets Space*, 69, 1–10, 2017.

Francis, S. H.: Global propagation of atmospheric gravity waves: A review, *J. Atmos. Terr. Phys.*, 37, 1011–1054, 1975.

Frissell, N. A., Kaepller, S. R., Sanchez, D. F., Perry, G. W., Engelke, W. D., Erickson, P. J., Coster, A. J., Ruohoniemi, J. M., Baker, J. B. H., and West, M. L.: First observations of large scale traveling ionospheric disturbances using automated amateur radio receiving networks, *Geophys. Res. Lett.*, 49, e2022GL097879, <https://doi.org/10.1029/2022GL097879>, 2022.

Fritts, D. C.: Gravity Wave Forcing and Effects in the Mesosphere and Lower Thermosphere, in: The Upper Mesosphere and Lower Thermosphere: A Review of Experiment and Theory, edited by: Johnson, R. M. and Killeen, T. L., American Geophysical Union, Washington, Geophysical Monograph 87, 89–100, 1995.

Galushko, V. G., V. S. Beley, V. S., Koloskov, A. V., Yampolski, Yu M., Paznukhov, V. V., Reinisch, B. W., Foster, J. C., and Erickson, P.: Frequency-and-angular HF sounding and ISR diagnostics of TIDs, *Radio Sci.*, 38, 1102, <https://doi.org/10.1029/2002RS002861>, 2003.

Garcia, F. J., Kelley, M. C., Makela, J. J., and Huang, C.-S.: Airglow observations of mesoscale low-velocity traveling ionospheric disturbances at midlatitudes, *J. Geophys. Res.*, 105, 18407–18415, 2000.

Hernández-Pajares, M., Juan, J. M., Sanz, J., and Aragón-Ángel, A.: Propagation of medium scale traveling ionospheric disturbances at different latitudes and solar cycle conditions, *Radio Sci.*, 47, RS0K05, <https://doi.org/10.1029/2011RS004951>, 2012.

Hocke, K. and Schlegel, K.: A review of atmospheric gravity waves and travelling ionospheric disturbances: 1982–1995, *Ann. Geophys.*, 14, 917–940, <https://doi.org/10.1007/s00585-996-0917-6>, 1996.

Hocking, W. K.: Performing Fourier transforms on extremely long data streams, *Comput. Phys.*, 3, 59–65, 1989.

Houghton, J.: The Physics of Atmospheres, Cambridge University Press, Cambridge, United Kingdom, 116 pp., ISBN 0521804566, 2002.

Hunsucker, R. D.: Atmospheric gravity waves generated in the high-latitude ionosphere: A review, *Rev. Geophys.*, 20, 293–315, 1982.

Johnson, J. B., Arechiga, R. O., Thomas, R. J., Edens, H. E., Anderson, J., and Johnson, R., Imaging thunder, *Geophys. Res. Lett.*, 38, L19807, <https://doi.org/10.1029/2011GL049162>, 2011.

Joyner, E. H. and Butcher, E. C.: Gravity wave effects in the nighttime F-region, *J. Atmos. Terr. Phys.*, 42, 455–459, 1980.

Kelley, M. C.: On the origin of mesoscale TIDs at midlatitudes, *Ann. Geophys.*, 29, 361–366, <https://doi.org/10.5194/angeo-29-361-2011>, 2011.

Kotake, N., Otsuka, Y., Tsugawa, T., Ogawa, T., and Saito, A.: Climatological study of GPS total electron content variations caused by medium scale traveling ionospheric disturbances, *J. Geophys. Res.-Space*, 111, A04306, <https://doi.org/10.1029/2005JA011418>, 2006.

LaBelle, J.: Replication Data for: “Tracking Traveling Ionospheric Disturbances through Doppler-shifted AM radio transmissions”, Version V1, Harvard Dataverse [data set], <https://doi.org/10.7910/DVN/L3JXIH>, 2024.

Lacross, R. T., Kelly, E. J., and Toksoz, M. N.: Estimation of seismic noise structure using arrays, *Geophysics*, 34, 21–38, 1969.

Makela, J. J. and Otsuka, Y.: Overview of Nighttime Ionospheric Instabilities at Low- and Mid-Latitudes: Coupling Aspects Resulting in Structuring at the Mesoscale, *Space Sci. Rev.*, 168, 419–440, 2011.

Martinis, C., Baumgardner, J., Wrotten, J., and Mendillo, M.: Seasonal dependence of MSTIDs obtained from 630.0 nm airglow imaging at Arecibo, *Geophys. Res. Lett.*, 37, L11103, <https://doi.org/10.1029/2010GL043569>, 2010.

Narayanan, V. L., Shiokawa, K., Otsuka, Y., and Neudegg, D.: On the role of thermospheric winds and sporadic E layers in the formation and evolution of electrified MSTIDs in geomagnetic conjugate regions, *J. Geophys. Res.-Space*, 123, 6957–6980, 2018.

Otsuka, Y., Suzuki, K., Nakagawa, S., Nishioka, M., Shiokawa, K., and Tsugawa, T.: GPS observations of medium-scale traveling ionospheric disturbances over Europe, *Ann. Geophys.*, 31, 163–172, <https://doi.org/10.5194/angeo-31-163-2013>, 2013.

Park, J., Luhr, H., Min, K., and Lee, J.: Plasma density undulations in the nighttime mid-latitude F-region as observed by CHAMP, KOMPSAT-1 M, and DMSP F15, *J. Atmos. Sol.-Terr. Phys.*, 72, 183–192, <https://doi.org/10.1016/j.jastp.2009.11.007>, 2010.

Paznukhov, V. V., Galushko, V. G., and Reinisch, B. W.: Digisonde observations of TIDs with frequency and angular sounding technique, *Adv. Space Res.*, 49, 700–710, 2012.

Perkins, F.: Spread F and ionospheric currents, *J. Geophys. Res.*, 78, 218–226, 1973.

Ransom, S. M., Eikenberry, S. M., and Middleditch, J.: Fourier techniques for very long astrophysical time-series analysis, *Astron. J.*, 124, 1788–1809, 2002.

Reznychenko, A. I., Koloskov, A. V., Sopin, A. O., and Yampolski, Y. O.: Statistic of Seasonal and Diurnal Variations of Doppler Frequency Shift of HF Signals at Mid-Latitude Radio Path, *Radio Physics and Radio Astronomy*, 25, 118–135, 2020.

Richmond, A. D.: Gravity wave generation, propagation, and dissipation in the thermosphere, *J. Geophys. Res.*, 83, 4131–4145, 1978.

Sears, R. D.: Ionospheric HF Doppler dispersion during the eclipse of 7 March 1970 and TID analysis, *J. Atmos. Terr. Phys.*, 34, 727–732, 1972.

She, C.-Y., Yan, Z.-A., Gardner, C. S., Krueger, D. A., and Hu, X.: Climatology and seasonal variations of temperatures and gravity wave activities in the mesopause region above Ft. Collins, CO (40.6° N, 105.1° W), *J. Geophys. Res.-Atmos.*, 127, e2021JD036291, <https://doi.org/10.1029/2021JD036291>, 2022.

Shibata, T. and Okuzawa, T.: Horizontal velocity dispersion of medium-scale travelling ionospheric disturbances in the F-region, *J. Atmos. Terr. Phys.*, 45, 149–159, 1983.

Shiokawa, K., Ihara, C., Otsuka, Y., and Ogawa, T.: Statistical study of nighttime medium-scale traveling ionospheric disturbances using midlatitude airglow images, *J. Geophys. Res.-Space*, 108, 1052, <https://doi.org/10.1029/2002JA009491>, 2003.

Tanaka, T., Ichinose, T., Okuzawa, T., Shibata, T., Sato, Y., Nagasawa, C., and Ogawa, T.: HF-Doppler observations of acoustic waves excited by the Urakawa-Oki earthquake on 21 March 1982, *J. Atmos. Terr. Phys.*, 46, 233–245, 1984.

Tedd, B. L., Strangeways, H. J., and Jones, T. B.: The influence of large-scale TIDs on the bearings of geographically spaced HF transmissions, *J. Atmos. Terr. Phys.*, 46, 109–117, 1984.

Toman, K.: On wavelike perturbations in the F region, *Radio Sci.*, 11, 107–119, 1975.

Tsuboi, T., Shiokawa, K., Otsuka, Y., Fujinami, H., and Nakamura, T.: Statistical Analysis of the Horizontal Phase Velocity Distribution of Atmospheric Gravity Waves and Medium-Scale Traveling Ionospheric Disturbances in Airglow Images Over Sata (31.0° N, 130.7° E), Japan, *J. Geophys. Res.-Space*, 128, e2023JA031600, 2023, <https://doi.org/10.1029/2023JA031600>, 2023.

Tsugawa, T., Saito, A., and Otsuka, Y.: A statistical study of large-scale traveling ionospheric disturbances using the GPS network in Japan, *J. Geophys. Res.-Space*, 109, A06302, <https://doi.org/10.1029/2003JA010302>, 2004.

Tsugawa, T., Otsuka, Y., Coster, A. J., and Saito, A.: Medium scale traveling ionospheric disturbances detected with dense and wide TEC maps over North America, *Geophys. Res. Lett.*, 34, L22101, <https://doi.org/10.1029/2007GL031663>, 2007.

Tsutsui, M., Horikawa, T., and Ogawa, T.: Determination of velocity vectors of thermospheric wind from dispersion relations of TID's observed by an HF Doppler array, *J. Atmos. Terr. Phys.*, 46, 447–462, 1984.

Yakovets, A. F., Vodyannikov, V. V., Andreev, A. B., Gordienko, G. I., and Litvinov, Y. G.: Features of statistical distributions of large-scale traveling ionospheric disturbances over Almaty, *Geomagn. Aeronomy+*, 51, 640–645, 2011.

Yeh, K. C. and Liu, C. H.: Acoustic-gravity waves in the upper atmosphere, *Rev. Geophys.*, 12, 193–216, 1974.

Zhang, S.-R., Erickson, P. J., Goncharenko, L. P., Coster, A. J., Rideout, W., and Vierinen, J.: Ionospheric bow waves and perturbations induced by the 21 August 2017 solar eclipse, *Geophys. Res. Lett.*, 44, 12067–12073, <https://doi.org/10.1002/2017GL076054>, 2017.

Zhang, S.-R., Coster, A. J., Erickson, P. J., Goncharenko, L. P., Rideout, W., and Vierinen, J.: Traveling ionospheric disturbances and ionospheric perturbations associated with solar flares in September 2017, *J. Geophys. Res.-Space*, 124, 5894–5917, 2019.

Zhang, S.-R., Nishimura, Y., Erickson, P. J., Ercha, A., Kil, H., Deng, Y., Thomas, E. G., Rideout, W., Coster, A. J., Kerr, R., and Vierinen, J.: Traveling Ionospheric Disturbances in the Vicinity of Storm-Enhanced Density at Midlatitudes, *J. Geophys. Res.-Space*, 127, e2022JA030429, <https://doi.org/10.1029/2022JA030429>, 2022.